Unveiling Chemical Enrichment in the Abell 2029 Core with XRISM, XMM-Newton, and Chandra

Arnab Sarkar, 1,2 Eric D. Miller, 1 Brian McNamara, 3 Ming Sun, 4 Richard Mushotzky, 5 Stefano Ettori, 6,7 Lorenzo Lovisari, 8,9 Irina Zhuravleva, 10 and Naomi Ota 11

¹ Kavli Institute for Astrophysics and Space Research, Massachusetts Institute of Technology, 70 Vassar St, Cambridge, MA 02139, USA
 ² Department of Physics, University of Arkansas, 825 W Dickson st., Fayetteville, AR 72701, USA
 ³ Department of Physics & Astronomy, Waterloo Centre for Astrophysics, University of Waterloo, Ontario N2L 3G1, Canada
 ⁴ Department of Physics and Astronomy, The University of Alabama in Huntsville, Huntsville, AL 35899, USA
 ⁵ Department of Astronomy, University of Maryland, College Park, MD 20742, USA
 ⁶ INAF, Osservatorio di Astrofisica e Scienza dello Spazio, via Piero Gobetti 93/3, 40129 Bologna, Italy
 ⁷ INFN, Sezione di Bologna, viale Berti Pichat 6/2, 40127 Bologna, Italy
 ⁸ INAF, Istituto di Astrofisica Spaziale e Fisica Cosmica di Milano, via A. Corti 12, 20133 Milano, Italy
 ⁹ Center for Astrophysics | Harvard & Smithsonian, 60 Garden Street, Cambridge, MA 02138, USA
 ¹⁰ Department of Astronomy and Astrophysics, University of Chicago, Chicago, IL 60637, USA
 ¹¹ Department of Physics, Nara Women's University, Nara 630-8506, Japan

ABSTRACT

We present new measurements of the chemical abundance pattern in the core of the nearby galaxy cluster Abell 2029, based on XRISM observations with Resolve (37 ks) and Xtend (500 ks), combined with archival data from XMM-Newton (EPIC, RGS) and Chandra. Fe abundances derived from Resolve, Xtend, and EPIC are broadly consistent, while RGS gives systematically lower values. Because the XRISM gate valve remained closed during these observations, Resolve spectral fitting is restricted to the 2–10 keV band, providing reliable constraints only for elements with strong lines in this band (S, Ar, Ca, Fe, Ni). Abundances of the α -elements are therefore derived using complementary observations from Xtend, EPIC, RGS, and Chandra. We construct an average X/Fe pattern in the cluster core by using Resolve exclusively for S/Fe, Ar/Fe, Ca/Fe, and Ni/Fe, and RGS + Xtend for O/Fe. The Ne/Fe ratio is averaged from Xtend, EPIC, RGS, and Chandra measurements; Mg/Fe from EPIC and Chandra measurements; and Si/Fe from Xtend, EPIC, and Chandra. Comparison with the supernovae yield models indicates that the observed abundance pattern in A2029 core is best reproduced by a combination of core-collapsed yields from low-metallicity progenitors ($Z_{\text{init}} = 0.001$) and a sub-Chandrasekhar-mass, double-degenerate Type Ia model. Additionally, we find an excess in Ca abundance in the core of A2029 that cannot be reproduced by the standard supernovae yield models.

Keywords: Galaxy cluster — ICM — X-ray — Abundance

1. INTRODUCTION

High-resolution X-ray spectroscopy serves as a powerful tool to precisely measure the chemical abundances of the intra-cluster medium (ICM) in galaxy clusters. The observed emission lines primarily arise from K-and L-shell transitions in highly ionized, hot plasma (e.g., Chakraborty et al. 2020a,b; de Plaa et al. 2017; Simionescu et al. 2019; Fukushima et al. 2023). The Re-

solve X-ray microcalorimeter on board XRISM (Tashiro et al. 2020; Ishisaki et al. 2022), with its ~ 4.5 evlevel spectral resolution, enables high-fidelity and precise measurements of ICM chemical abundances by resolving individual K-shell emission lines. However, under the gate-valve-closed configuration, the practical energy band for extended sources is limited to > 2 keV. Consequently, metal abundance measurements by Resolve are currently restricted to the He- and H-like $K\alpha$ complexes of Si, S, Ar, Ca, Cr, Mn, Fe, and Ni (i.e., Fe-peak elements). Within this band, Resolve's eV-level resolving power cleanly separates blends in the

weak Fe-peak K lines (Cr, Mn, Ni) that are otherwise blended with Fe features, allowing robust Fe-peak/Fe abundance ratios that directly probe Type Ia supernova enrichment channels. Several XRISM Performance Verification (PV)-phase observations of nearby clusters confirm strong detections of these K-shell lines (e.g., XRISM Collaboration et al. 2025a; Sarkar et al. 2025; XRISM Collaboration et al. 2025b; Fujita et al. 2025; XRISM Collaboration et al. 2025c).

With a better understanding of stellar nucleosynthesis over the past decades, it is now evident that most of the lighter elements, like O, Mg, and Ne, are synthe sized by massive stars ($\sim 10-140~M_{\odot}$) and expelled into the ICM by core-collapse supernovae (SNcc; e.g., Nomoto et al. 2006, 2013). On the other hand, the heavier elements, like Ar, Ca, Fe, and Ni, are primarily produced by Type Ia supernovae (SNe Ia; e.g., Iwamoto et al. 1999; Mernier et al. 2016b; Sarkar et al. 2022). For decades, the SNIa yield models have predominantly focused on scenarios involving a carbon-oxygen white dwarf (WD) that approaches the Chandrasekhar limit either through stable hydrogen-rich accretion from a non-degenerate companion (single degenerate; Whelan & Iben 1973), or through the violent merger of two C/O WDs (double degenerate; Iben & Tutukov 1984). In such models, central carbon ignition initiates a simmering phase, which is subsequently followed by the onset of a deflagration, a transition to detonation, and ultimately a thermonuclear explosion (e.g., Plewa et al. 2004; Seitenzahl et al. 2013).

More developments from last decade have shown that helium-accreting systems, particularly those involving helium white dwarf donors, can lead to significantly smaller helium shells at ignition due to higher accretion rates (Bildsten et al. 2007; Shen & Bildsten 2009). These insights have led to a renewed interest in sub-Chandrasekhar-mass (sub-M_{Ch}) explosions, particularly in the context of double-detonation models (e.g., Fink et al. 2010; Kromer et al. 2010; Woosley & Kasen 2011; Shen & Bildsten 2014). Parallel studies of dynamically unstable WD mergers have also suggested that helium detonation may be triggered during the merger phase itself, as mass is rapidly transferred (e.g., Guillochon et al. 2010; Pakmor et al. 2013). This pathway has gained further traction, but it is not yet fully understood. While the nature of SN Ia progenitors remains a long-standing open question in astrophysics, it is evident that the detailed abundance patterns of the metals produced are intimately linked to the physics of the explosion mechanism (e.g., Maoz & Mannucci 2012; Maoz et al. 2014; Shen et al. 2018; Ruiter & Seitenzahl 2025).

Galaxies are open systems, gaining pristine gas and losing enriched gas, making their remaining metallicity highly model dependent. Metals produced within cluster member galaxies accumulate in the ICM over very long periods (> 5 Gyr) and represent a true average over many individual galaxies. The total mass of metals deposited in the cluster core is approximately 2–6 times greater than the metal mass retained within the galaxies themselves (Renzini & Andreon 2014; Mernier et al. 2018a; Gastaldello et al. 2021; Molendi et al. 2024). As a result, the metal abundances in the ICM serve as a "fossil" record of the cumulative yields from successive generations of stars, released through supernova explosions and stellar winds. These abundance patterns offer a unique test bed to constrain SNcc and SNIa yield models as well as other aspects of star formation, IMF and galactic winds.

This paper (Paper IV of the Abell 2029 XRISM PV observation series), focuses on the chemical enrichment in the core of Abell 2029 galaxy cluster. To constrain the abundances of low-energy α -elements, we supplement the Resolve data with simultaneous XRISM Xtend observations and with archival observations from XMM-Newton RGS and EPIC, as well as Chandra ACIS. Together, we derive elemental abundances for nine elements: O, Ne, Mg, Si, S, Ar, Ca, Fe, and Ni. Throughout this work, we adopt a Λ CDM cosmology with $H_0 =$ 70 km s⁻¹ Mpc⁻¹, $\Omega_m = 0.3$, and $\Omega_{\Lambda} = 0.7$. At the redshift of Abell 2029 (z = 0.0787), 1' corresponds to 89 kpc. We adopt the proto-solar abundance table of Lodders & Palme (2009) throughout. Unless otherwise noted, all uncertainties are reported at the 1σ (68%) confidence level.

2. DATA REDUCTION

2.1. XRISM/Resolve

XRISM observed the central region of Abell 2029 through two co-aligned pointings on 2024 January 10 and 13, with exposure times of 12.44 ks (OBSID 000149000) and 25.11 ks (OBSID 000151000), respectively. Two additional offset pointings were conducted: North 1, observed between 2024 January 10–13 for 106.03 ks (OBSID 000150000), and North 2, observed between 2024 July 27 and August 4 for 366.15 ks (OBSID 300053010). A complete observation log is provided in Table 1. In this work, we utilize data from both the Resolve and Xtend instruments. The data were reprocessed using HEASoft v6.34 and the most recent calibration database (CalDB v20250915), following the standard screening procedures adopted in the XRISM analysis of N132D (XRISM Collaboration 2024).

Table 1	1. Ob	servation	logs
---------	-------	-----------	------

Telescope	$Instrument^{\dagger}$	Pointing	Observation ID	RA	Decl.	Observation Date	Exposure
				(deg)	(deg)		(ks)
	Resolve/Xtend	Central	000149000	227.7341	5.7451	2024-01-10	12.44
XRISM	Resolve/Xtend	Central	000151000	227.7331	5.7450	2024-01-13	25.11
	Xtend	North 1	000150000	227.7635	5.7850	2024-01-10	106.03
	Xtend	North 2	300053010	227.7943	5.8245	2024-07-27	366.15
XMM-Newton	PN/MOS/RGS	_	0111270201	227.7333	5.7450	2002-08-25	23.5
	$\mathrm{PN}/\mathrm{MOS}/\mathrm{RGS}$	_	0551780201	227.7447	5.7616	2008-07-17	46.8
	$\mathrm{PN}/\mathrm{MOS}/\mathrm{RGS}$	_	0551780301	227.7447	5.7619	2008-07-19	46.8
	$\mathrm{PN}/\mathrm{MOS}/\mathrm{RGS}$	_	0551780401	227.7447	5.7616	2008-07-21	46.8
	$\mathrm{PN}/\mathrm{MOS}/\mathrm{RGS}$	_	0551780501	227.7447	5.7616	2008-07-18	33.5
Chandra	ACIS-S	_	891	227.7267	5.7636	2000-04-12	19.8
	ACIS-I	_	6101	227.7632	5.7636	2004-12-17	9.9
	ACIS-S	_	4977	227.7469	5.7582	2004-12-17	76.8

[†] Instrument data analyzed in this paper.

For detailed data reduction methods for Resolve, we refer readers to Paper I (XRISM Collaboration 2025), Paper II (XRISM Collaboration et al. 2025a), and Paper III (Sarkar et al. 2025). In summary, energy-scale drift in Resolve during observations is tracked by periodically illuminating the focal plane with a built-in ⁵⁵Fe source mounted on the filter wheel, typically during Earth occultation. After gain reconstruction, the flat-field-averaged energy scale uncertainty is estimated to be ± 0.3 eV in the 5.4–9 keV band, based on inorbit calibration using Cr and Cu lines from a modulated X-ray source and Mn from the ⁵⁵Fe source. To assess the energy-scale correction for individual observations, a dedicated calibration pixel—positioned outside the aperture and continuously exposed to a collimated ⁵⁵Fe source—was used. Gain reconstruction for this pixel relied solely on data from fiducial intervals applied to the main array, while the Mn K α 5.9 keV line was fitted during non-fiducial times to emulate a celestial observation (XRISM Collaboration 2024). The largest residual line offset was found to be 0.12 eV in OBSID 000149000, which should be added in quadrature to the 0.3 eV systematic uncertainty.

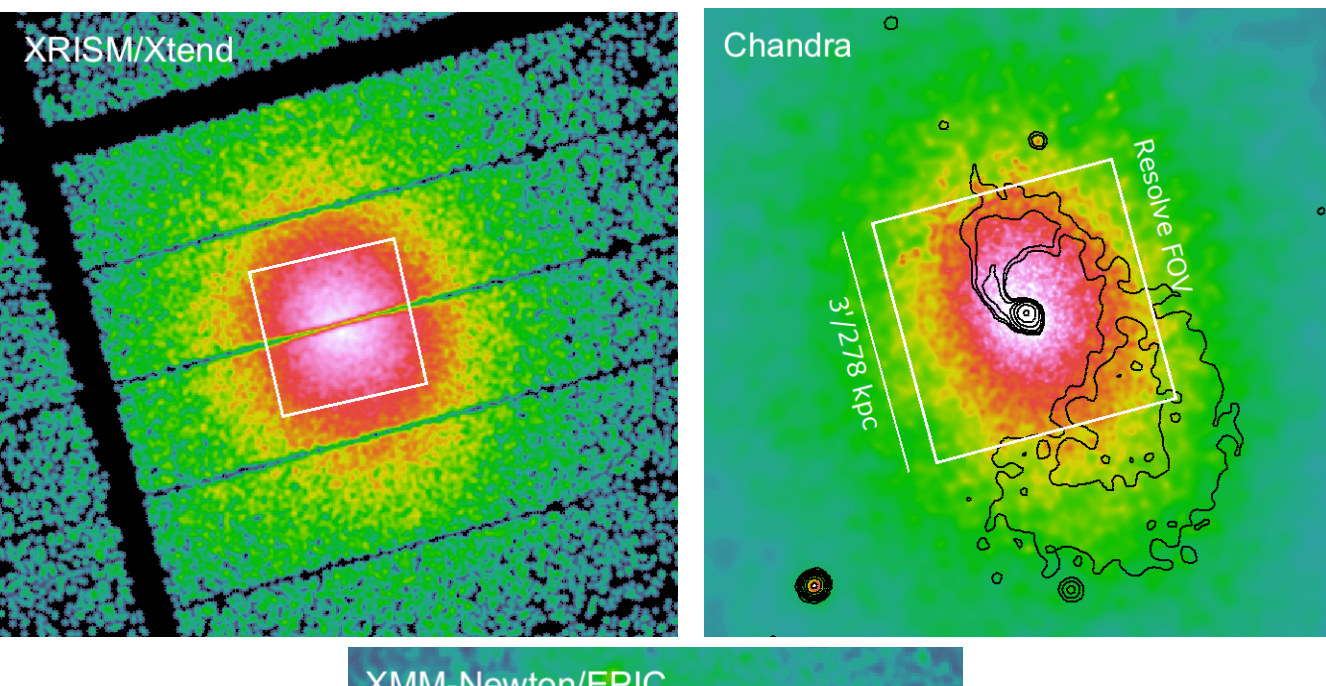
For each observation, spectra were extracted from the full array, excluding pixel 27, which exhibited anomalous gain shifts not aligned with the timing of the ⁵⁵Fe fiducial exposures. Pixel 11 also occasionally displays similar abrupt scale variations, therefore, excluded in our analysis (Sarkar et al. 2025). Our analysis includes only high-resolution primary (Hp; ITYPE=0) events, which comprise more than 99% of the 2–10 keV event population in each observation. Low-resolution secondary (Ls; ITYPE=4) events, typically associated with instrumen-

tal effects at these low count rates, were excluded. For background, a non-X-ray background (NXB) spectrum was generated for each observation using the rslnxbgen tool. The NXB was constructed from the Resolve night-Earth database, applying identical screening criteria as for the source data. Weighting was applied according to the geomagnetic cut-off rigidity distribution sampled during the respective observation.

Instrumental responses were generated for each observation using rslmkrmf with the most up-to-date calibration database (CalDB v20250915). The redistribution matrix file (RMF) was scaled by the fraction of high-resolution primary (Hp) events in the 2–10 keV band—excluding low-resolution secondary (Ls) events—to properly account for the exclusion of medium- and low-resolution events and ensure accurate flux normalization. Ancillary response files (ARFs) were created using xaarfgen, with an exposure-corrected, full-resolution Chandra image in the 2–8 keV band serving as the input source model, as shown in Figure 1 (right).

2.2. XRISM/Xtend

The data reduction procedure for Xtend follows the methodology described in Sarkar et al. (2025). Briefly, the first step involved identifying and removing flickering pixels from the event file. These pixels, characterized by abnormally high counts due to interactions with high-energy cosmic rays and charged particles, were filtered out by running the searchflickpix tool twice. This approach was necessary because the updated version of xtdflagpix, which incorporates flickering pixel removal, had not yet been released as part of HEASoft



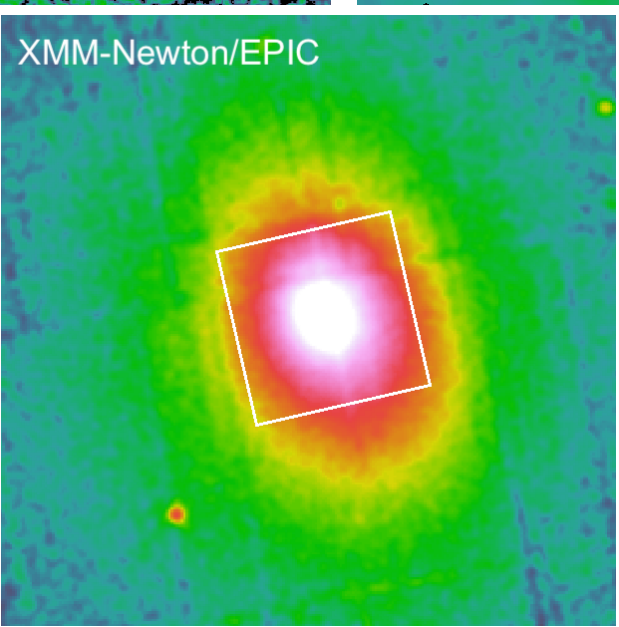


Figure 1. Top-Left: XRISM/Xtend count image of A2029 in the 0.6–10 keV energy band. Top-Right: Exposure-corrected, background-subtracted Chandra ACIS-I image of A2029 in the 0.5–7 keV energy band. Black surface brightness contours highlight the cold-gas sloshing spiral in the cluster center. Bottom: Exposure corrected, QPB-subtracted, merged XMM-Newton EPIC image of A2029. White boxes in all three panels represent the XRISM/Resolve field of view (FOVs) used to extract spectra from all three instruments.

v6.34. Following this, the calibration sources located on either side of the Xtend field of view (FoV) were masked. The event file, now cleaned of flickering pixels and with calibration sources masked, was used to extract an image in the 0.6–10 keV band, as shown in Figure 1 (left). A spectrum was extracted from a rectangular region corresponding to the Resolve field of view, also indicated in Figure 1 (left).

The response matrix file (RMF) was generated using xtdrmf, and two ancillary response files (ARFs) were created with xaarfgen. One ARF was produced using the IMAGE mode, which incorporates a full-resolution Chandra image as the source input; the second used the FLATCIRCLE mode with a fixed radius of 15'. The IMAGE-mode ARF was applied to model the source spectra, while the FLATCIRCLE-mode ARF was used to model the sky background (see Paper III for more

details; Sarkar et al. 2025). The non-X-ray background was modeled using a power-law component to represent the quiescent background, along with several Gaussian lines, as also discussed in Paper III (see Section 2.3).

2.3. XMM-Newton/EPIC

We incorporated archival XMM-Newton EPIC data in this analysis, with the full list of observation IDs provided in Table 1. Data reduction was carried out using the XMM-Newton Extended Source Analysis Software (XMM-ESAS*) and associated procedures for processing EPIC (European Photon Imaging Camera) observations. Event files were first calibrated and filtered with the standard XMM-ESAS tasks epchain, emchain, mos-filter, and pn-filter, applying the most recent Current Calibration Files (CCF) database. Soft-proton flares were removed using high-energy (2.5–12 keV) light curves derived from the unexposed detector corners. From the cleaned event lists, images were created in the 0.7-1.2 keV band for point-source detection. Corresponding exposure maps were generated for each detector to correct for chip gaps and mirror vignetting. Point sources were identified with the automated XMM-ESAS task cheese-bands and excluded from subsequent analysis. Quiescent particle background (QPB) images were then constructed from filter-wheel-closed data using the mos-back and pn-back tools (Snowden et al. 2008). The final exposure-corrected, QPB-subtracted image of A2029 is shown in Figure 1 (bottom).

For each observation, MOS1, MOS2, and pn spectra were extracted from a 3' × 3' region matching Resolve FoV (see Figure 1), using ESAS task evselect. Redistribution matrix files (RMF) were produced using rmfgen, and ancillary response files were generated with arfgen task. The QBP spectra were constructed using mos-back for MOS1 and MOS2 and pn-back for the pn instrument. The hard particle background was modeled following Mernier et al. (2015).

$2.4. \ XMM-Newton/RGS$

XMM-Newton/RGS data reduction was carried out with the same ESAS package as that of EPIC. All RGS data sets were reprocessed using rgsproc, following the standard procedures recommended by the SAS team. Periods contaminated by solar flares were filtered using rgsfilter, by selecting background-quiescent intervals in the lightcurves of the RGS 1 and 2 from CCD number 9. A count rate threshold of ~ 0.2 c/s was applied, and the resulting clean exposure times are listed in Table 1.

First- and second-order RGS spectra were extracted from a cross-dispersion region of width 0.8', centered on the source coordinates (RA = 227.7328° , Dec = $+5.7449^{\circ}$). Background spectra were constructed from photons lying beyond the 98% source point-spread function boundary; we verified that these regions never overlapped with the bright source. The rgsproc task simultaneously generated the associated response files for both RGS1 and RGS2. In this study, we only considered the first-order spectra from both RGS instruments.

2.5. Chandra

We also analyzed three Chandra observations from 2000 to 2004, with the Obs ID 891, 4977 and 6101, as reported in Table 1. There were deep Chandra ACIS-I observations in 2022 - 2023 for the cluster, with a total clean exposure time of 404.3 ks. However, the newer data require additional calibration and are in fact not much deeper than the old data because of the degradation of Chandra's response at the soft X-rays. At the 0.5-7 keV band, the 2022-2023 data are only ~ 1.33 times deeper than the old data, measured within 10'' radius from the cluster center. Therefore, our studies focus on the 2000-2004 data.

We reduced the Chandra ACIS observations with the Chandra Interactive Analysis of Observation (CIAO; version 4.17) and calibration database (CALDB; version 4.12.0). Standard ACIS data reduction was followed, which includes running chandra_repro, data mode filtering, and removal of background flares. Updated type 2 event files with clean exposure were then generated. The total clean exposure time is 106.5 ks. We extracted the Chandra spectra within 1.5′ from the center and fit three spectra simultaneously. The background is taken from the blank sky background, with the 9.5 - 12 keV flux normalized by the values during the A2029 observations. All the setup for the spectral analysis is the same as for the other data.

3. SPECTRAL FITTING

We utilized the XSPEC v12.15.0 fitting package to perform the spectral analysis (Arnaud 1996). All spectra were fitted by minimizing the C-statistics (Cash 1979) to estimate the model parameters and their uncertainty range. We assumed that the ICM is in collisional ionization equilibrium (CIE) state and therefore can be modeled using the AtomDB (v3.1.0 †). The abundances were calculated from all the transitions and ions of a given element, and are scaled to the proto-solar values of Lodders & Palme (2009). Several previous studies have

^{*} https://heasarc.gsfc.nasa.gov/docs/xmm/abc/

[†] http://www.atomdb.org

shown that fitting a multi-phase plasma with a single-temperature model can lead to a systematic underestimation of the Fe abundance (e.g., Gastaldello et al. 2021; Sarkar et al. 2022). In Paper III (Sarkar et al. 2025), we demonstrated that multi-temperature gas exists within $3' \times 3'$ Resolve field of view at the core of A2029. We, therefore, adopted a two-temperature (2T) CIE model in our spectral analysis to mitigate this Fe bias.

For fitting the Resolve spectra, we followed the same procedure as described in (Sarkar et al. 2025). The spectra were modeled with two BVAPEC components. The temperatures and normalizations of both components were allowed to vary, while individual elemental abundances, redshift, σ_v (the line-of-sight broadening of the lines) were varied jointly between two components. All parameters were tied between two OBS IDs. We also modeled instrumental background and sky-background (such as CXB and galactic halo) simultaneously with the source model. We refer readers to (Sarkar et al. 2025) for more details on individual background models. Due to the loss of spectral sensitivity below 2 keV band, we fitted Resolve spectra within 2–10 keV energy band. This choice of spectral band does not allow to constrain the abundances of O, Ne, Mg, and Si. We, therefore, tied these elements to Fe while fitting. Figure 2 (top-left) shows the Resolve spectra of A2029 with the best-fit model.

Xtend spectral fitting was performed in the 0.6–10 keV energy band, as recommended in the quick start guide[‡]. We fitted Xtend spectra with two VAPEC components for ICM emission simultaneously with the NXB and sky background models, following the same strategy as Sarkar et al. (2025). Figure 2 (top-right) panel shows the Xtend spectra for the A2029 core alongwith the best-fit model. The temperature and normalizations of both components were free to vary however tied between OBS IDs. The elemental abundances of O, Ne, Si, S, Fe, and Ni were varied jointly between two VAPEC components. The redshift parameter was fixed to the best-fit value (z = 0.07776) obtained from Resolve spectral fitting.

We analyzed archival XMM-Newton EPIC and RGS observations to complement XRISM measurements. For the EPIC, the MOS and pn spectra from all OBS IDs were fitted simultaneously using two VAPEC components for the ICM emission and a full background model for the sky background (including cosmic X-ray background and galactic foreground components), similar to the Xtend. The temperature of two VAPEC com-

ponents were free to vary however were tied between MOS and pn as well as between all OBS IDs. However, normalization components were free to vary for all components, instruments, and OBS IDs. The elemental abundances of O, Ne, Mg, Si, S, Fe, and Ni were varied collectively between instruments and OBS IDs. Previous XMM-Newton studies such as Schellenberger et al. (2015) reported extremely variable soft tail in the EPIC filter wheel closed events that might considerably affect the spectra below 0.5 keV. Mernier et al. (2016a) found a good compromise by fitting the MOS spectra within 0.5–7 keV band and pn spectra within 0.6–7 keV band. We followed the same in this paper, as presented in Figure 2 (middle-left).

For this paper we only consider the first order spectra for XMM-Newton/RGS. Spectra from RGS 1 and RGS 2 instruments for all OBS IDs were fitted simultaneously with two VAPEC components to model the ICM emission. For each spectrum, we took into account the spectral broadening effect due to the spatial extent of the source by using the rgsxsrc multiplicative model in XSPEC and supplying MOS images. The temperature of the hotter component was free to vary, tied between instruments and OBS IDs. The cooler temperature component was linked to the hotter component as $kT_{\text{hot}}: kT_{cool} = 1:0.25$, following Fukushima et al. (2023). We did not adopt any assumption regarding the emission measures of each temperature component, therefore, left it free to vary. The spectral fitting was performed in the 0.2–2.0 KeV energy band. Due the limited spectral coverage of RGS, the elemental abundances of O, Ne, Mg, Si, and Fe were varied freely and other elements collectively with Fe, however all were tied between two VAPEC components. The redshift parameters were fixed to the best-fit value obtained from Resolve spectral fitting. Figure 2 (middle-right) shows the RGS 1 and RGS 2 spectra summed over all OBS IDs along with the best-fit models.

For the Chandra ACIS, we followed the similar fitting strategy as EPIC and Xtend. We modeled ACIS spectra with two absorbed VAPEC components to model the source emission. Figure 2 (bottom) shows the ACIS spectra from the central region of A2029 along with the best-fit model. The elemental abundances of O, Ne, Mg, Si, S, Fe, and Ni were free to vary but tied between two temperature components. The best-fit parameters are listed in Table 2.

For each spectral fitting described above, to account for the Galactic neutral column density along the line of sight, we applied the multiplicative phabs absorption model in XSPEC along with CIE components (Wilms et al. 2000). The absorption cross sections were adopted

[‡] https://heasarc.gsfc.nasa.gov/docs/xrism/analysis/quickstart

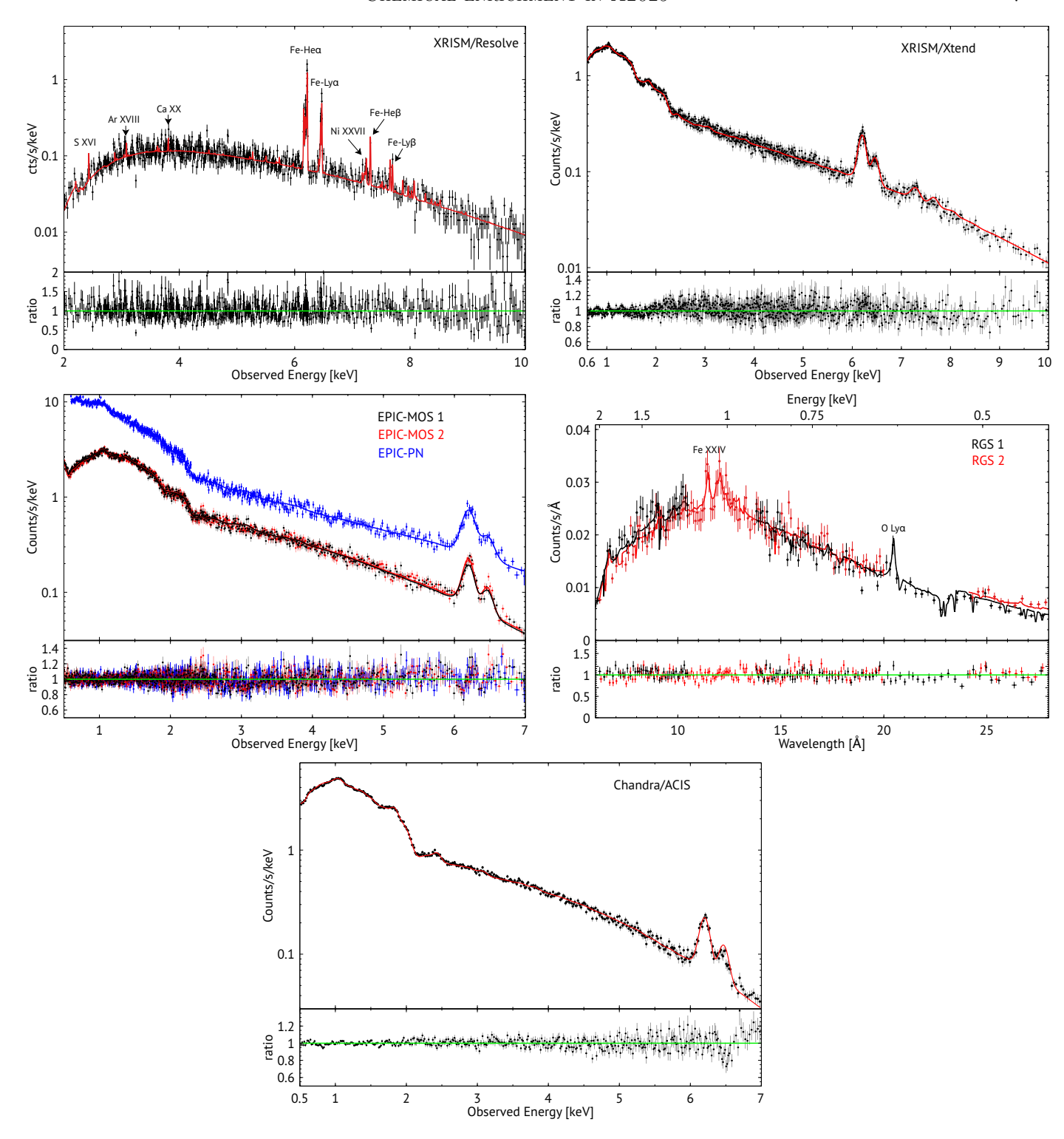


Figure 2. Top-Left: XRISM/Resolve full-array spectrum of A2029 (except pixels 12 and 27) from the central region, shown along with the best-fit model (red:total, blue:NXB). Top-Right: XRISM/Xtend spectrum from the central $3' \times 3'$ region (matching Resolve FoV) of A2029 with best-fit model (red). Middle-Left: EPIC/MOS1 (black), EPIC/MOS2 (red), and EPIC/pn (blue) spectra from the similar region used for Xtend, with best-fit models. Middle-Right: RGS1 (black) and RGS2 (red) first-order spectra extracted from a cross-dispersion region of 0.8', with best-fit models. Bottom: Chandra/ACIS spectrum of A2029 from the central $3' \times 3'$ region, with the best-fit model. For each instrument, the spectra from multiple observations have been combined to plot a single spectrum. In all panels, the lower sub-panels show the ratio between the observed data and the best-fit total models.

from Verner et al. (1996). We fixed to the galactic value, i.e., $N_{\rm H}=3\times10^{20}~{\rm cm}^{-2}$ (HI4PI Collaboration et al. 2016).

4. RESULTS

4.1. Temperature measurement

The best-fit temperatures from Resolve spectral fitting indicate the presence of two components: cooler phase at $4.81^{+0.62}_{-0.42}$ keV and a hotter phase at $8.97^{+2.77}_{-0.65}$ keV. The corresponding redshift ($z = 0.07776^{+0.00004}_{-0.00003}$) and velocity dispersion ($\sigma_v = 155^{+11}_{-11}$ $\rm km~s^{-1})$ are consistent with previous XRISM studies (e.g., Sarkar et al. 2025; XRISM Collaboration et al. 2025a; XRISM Collaboration 2025). The best-fit Xtend temperatures—5.85 $^{+0.52}_{-0.47}$ keV and 10.66 $^{+0.64}_{-0.65}$ keV—are also in agreement with those measured by Resolve and earlier XRISM studies. Similarly, the cooler gas temperature measured by EPIC $(4.60^{+0.11}_{-0.15} \text{ keV})$ and hotter gas temperature measured by RGS $(4.40^{+0.11}_{-0.10} \text{ keV})$ are consistent with the cooler gas found using Resolve and Xtend. The hotter temperature component from EPIC $(10.62^{+0.40}_{-0.39} \text{ keV})$ is likewise consistent with the hotter components measured by Resolve and Xtend. We note that the RGS spectral band is restricted to 0.2–2 keV. Therefore, it is not particularly sensitive to the hotter gas, which is better constrained by Resolve, Xtend, and EPIC. From Chandra spectral fitting, we obtain a cooler gas temperature of $5.32^{+0.37}_{-0.21}$ keV, in agreement with the gas temperatures found by Resolve, Xtend, EPIC, and RGS. However, we find that the hotter gas temperature measured with Chandra $(12.9^{+1.47}_{-0.39} \text{ keV})$ is marginally higher than those measured by the other instruments. This is consistent with the trend found by Schellenberger et al. (2015) in a comparison of cluster temperatures measured by XMM-Newton and Chandra.

4.2. Elemental abundances

Figure 3 (left) shows the best-fit abundances of O, Ne, Mg, Si, S, Ar, Ca, Fe, and Ni within the central 3′ of A2029. The corresponding numerical values are listed in Table 2. Thanks to its exceptional spectral resolution, Resolve provides not only precise but also accurate measurements of abundances from emission lines due to its ability to more cleanly separate the lines from the underlying continuum compared to CCD instruments. The best-fit abundances measured with Resolve are: S = $0.60^{+0.18}_{-0.17} Z_{\odot}$, Ar = $0.34^{+0.21}_{-0.20} Z_{\odot}$, Ca = $0.62^{+0.22}_{-0.20} Z_{\odot}$, Fe = $0.68^{+0.04}_{-0.04} Z_{\odot}$, and Ni = $0.54^{+0.17}_{-0.15} Z_{\odot}$.

The Fe abundances measured by Resolve, Xtend, and XMM-Newton/EPIC are marginally consistent with each other. However, the Fe abundance derived from XMM-Newton/RGS is systematically lower than those

from other instruments. This discrepancy is expected and can be attributed to several factors. The RGS extraction region differs in angular coverage, and so this could reflect real spatial abundance variations. In addition, the RGS bandpass excludes the Fe-K complex, so the Fe abundance is solely constrained by the Fe-L lines, which are in a forest of additional spectral lines that complicate proper measurement of the continuum. Moreover, for extended sources like A2029, instrumental line broadening further degrades the RGS ability to distinguish line emission from continuum, leading to larger systematic uncertainties. Similar differences between RGS and EPIC Fe measurements have been reported in previous studies, such as de Plaa et al. (2017) and Mernier et al. (2016a) based on the CHEERS In contrast, Chandra yields a significantly higher Fe abundance of 0.90 ± 0.02 solar. Fe abundance in Perseus core measured with ACIS-S3, compared to EPIC, was also reported by Molendi & Gastaldello (2009). They attributed the difference to cross-calibration uncertainties in the 1-5 keV effective area rather than to a real variation in abundance. However, we adopt Chandra measurements in this analysis because the X/Fe ratios are consistent with those from other instruments.

Absolute elemental abundances are often more sensitive to systematic uncertainties than relative abundances. It is, therefore, generally more reliable to examine abundance ratios relative to Fe (X/Fe). Figure 3 (right) presents the derived X/Fe abundance ratios for all measured elements at the core of A2029. The O/Fe ratios measured by RGS, EPIC, and Chandra are consistent with each other but are marginally higher than that The Ne/Fe ratios from Xtend, derived from Xtend. EPIC, RGS, and Chandra agree within their 1σ uncertainties. We note that while EPIC provide robust constraints on many elemental abundances, measuring O and Ne remains challenging. The O VIII emission line lies near ~ 0.6 keV. The EPIC spectral fitting were restricted to > 0.5 keV for MOS and > 0.6 keV for pn, close to the instrumental oxygen absorption edge, where calibration uncertainties can be significant. Additionally, the Ne K-shell lines overlap with the Fe-L complex, making Ne abundance measurements highly sensitive to assumptions about the ICM temperature structure.

The Mg/Fe abundance ratios are consistent between the EPIC and Chandra measurements. Although RGS yields an absolute Mg abundance that agrees with EPIC, its Mg/Fe ratio is marginally higher, driven by the systematically lower Fe abundance derived from RGS. For Xtend, we were unable to obtain a well-constrained Mg abundance; instead, we derive an 3σ upper limit of

Parameter	Resolve	Xtend	EPIC	RGS	Chandra
$kT_1 \text{ (keV)}$	$4.81^{+0.62}_{-0.42}$	$5.85^{+0.52}_{-0.47}$	$4.66^{+0.11}_{-0.15}$	$4.40^{+0.11}_{-0.10}$	$5.32^{+0.37}_{-0.21}$
$kT_2 \text{ (keV)}$	$8.97^{+2.77}_{-0.65}$	$10.66^{+0.64}_{-0.65}$	$10.62^{+0.40}_{-0.39}$	1.10^{d}	$12.9_{-1.45}^{+1.47}$
O	_	$0.58^{+0.16}_{-0.17}$	$1.03^{+0.08}_{-0.08}$	$0.57^{+0.06}_{-0.08}$	$1.14^{+0.18}_{-0.18}$
Ne	_	$0.50^{+0.15}_{-0.13}$	$0.86^{+0.12}_{-0.12}$	$0.36^{+0.15}_{-0.15}$	$0.66^{+0.16}_{-0.14}$
Mg	_	$< 0.35^{a}$	$0.74^{+0.06}_{-0.06}$	$0.70^{+0.16}_{-0.16}$	$0.72^{+0.13}_{-0.13}$
Si	_	$0.93^{+0.07}_{-0.06}$	$0.70^{+0.05}_{-0.05}$	$0.88^{+0.15}_{-0.15}$	$0.99^{+0.08}_{-0.08}$
S	$0.60^{+0.18}_{-0.17}$	$1.28^{+0.11}_{-0.09}$	$0.30^{+0.05}_{-0.05}$	_	$1.07^{+0.12}_{-0.11}$
Ar	$0.34^{+0.21}_{-0.20}$	_	_	_	_
Ca	$0.62^{+0.22}_{-0.20}$	_	_	_	_
Fe	$0.68^{+0.04}_{-0.04}$	$0.77^{+0.01}_{-0.01}$	$0.79^{+0.01}_{-0.01}$	$0.46^{+0.04}_{-0.04}$	$0.90^{+0.02}_{-0.02}$
Ni	$0.54^{+0.17}_{-0.15}$	$0.31^{+0.14}_{-0.10}$	$1.64^{+0.11}_{-0.11}$	$1.38^{+0.30}_{-0.30}$	$2.01^{+0.32}_{-0.32}$
Redshift	$0.07776^{+0.00004}_{-0.00003}$	0.07776^{b}	0.07776^{b}	0.07776^{b}	0.0777^{b}
$\sigma_v \; ({\rm km/s})$	155^{+11}_{-11}	_	_	_	_
$N_1 (10^{12} \text{ cm}^{-5})^c$	$1.85^{+0.78}_{-0.72}$	$2.09^{+0.4}_{-0.3}$	$1.85^{+0.15}_{-0.19}$	$2.40^{+0.15}_{-0.19}$	$0.04^{+0.03}_{-0.03}$
$N_2 (10^{12} \text{ cm}^{-5})^c$	$2.84^{+0.81}_{-0.57}$	$2.2^{+0.3}_{-0.3}$	$1.53^{+0.19}_{-0.15}$	< 0.003	$4.02^{+0.05}_{-0.05}$
Energy Band (keV)	2 – 10	0.6 – 10	0.5 - 7	0.2 - 2	0.5 - 7
C-stat/dof	3847/3846	5989/5737	17725/16698	3246/2935	1413/1318

Table 2. Best-fit parameters obtained by fitting spectra from the central region of A2029.

<0.35 solar, corresponding to Mg/Fe < 0.46. Si/Fe abundance ratios can be measured with relatively high precision using CCD instruments. As shown in Figure 3, the Si/Fe ratios derived from Xtend, EPIC, and Chandra are consistent. In contrast, RGS shows a systematically higher value. The Si XIII He-like triplet (at 1.865 keV) and Si XIV Ly α line (at \sim 2.0 keV) lie near the edge of the RGS bandpass, where the instrument's effective area declines rapidly. As a result, the Si/Fe ratios measured by RGS are less reliable for extended sources like A2029.

For the S/Fe, Ar/Fe, Ca/Fe, and Ni/Fe abundance ratios, we primarily leverage Resolve's superior spectral resolution and sensitivity, which offer significant advantages over CCD-based instruments. In addition to Fe He-like and H-like lines, S xv He-like triplet at \sim 2.46 keV, Ar xvII at \sim 3.12 keV, Ca xIX at \sim 3.90 keV, and Ni xxvII at \sim 7.8 keV are all clearly detected in the core of A2029 with Resolve. This capability allows for precise abundance measurements of these elements, which are otherwise blended with the continuum or neighboring lines in CCD spectra, where limited resolution and high instrumental background introduce substantial systematic uncertainties. Resolve clearly resolves the Ni–K α (w) line in the A2029 core (Figure 2), resulting in a sub-

solar Ni/Fe abundance ratio. Since, EPIC and Chandra spectral fitting were restricted to 7 keV and RGS can not resolve any Ni XXVI lines, the Ni abundance measured using these instruments are not reliable. Xtend, because of its orbit, benefits from a significantly lower instrumental background compared to EPIC, RGS, and Chandra, enabling a more reliable Ni abundance measurement that is in good agreement with Resolve.

Taking into account the strengths and limitations of each instrument, we adopt the following approach for the remainder of the analysis. For O/Fe, we use the average of RGS and Xtend measurements. For Ne/Fe, we adopt the average over Xtend, EPIC, RGS, and Chandra as these also show mutual agreement. The Mg/Fe ratio is averaged over EPIC and Chandra, while Si/Fe is averaged across Xtend, EPIC, and Chandra, excluding RGS due to its limited sensitivity to Si lines in extended sources. Finally, for S/Fe, Ar/Fe, Ca/Fe, and Ni/Fe, we adopt the values measured with Resolve. The adopted average X/Fe abundance ratios at the center of A2029 are shown in Figure 3 (right), marked in magenta.

4.3. Systematic uncertainty

We examine the measured chemical abundances in the core of A2029 for possible systematic biases. Because our analysis combines observations from multiple

 $a_{3\sigma}$ upper-limit

^b Redshift was fixed.

 $^{^{\}it C}$ The model normalization corresponds to a 3-arcmin diameter circular region centered on Abell 2029.

dThe temperature parameter was linked with the hotter component as $kT_{\text{hot}}: kT_{\text{cool}} = 1:0.25$, following Fukushima et al. (2023).

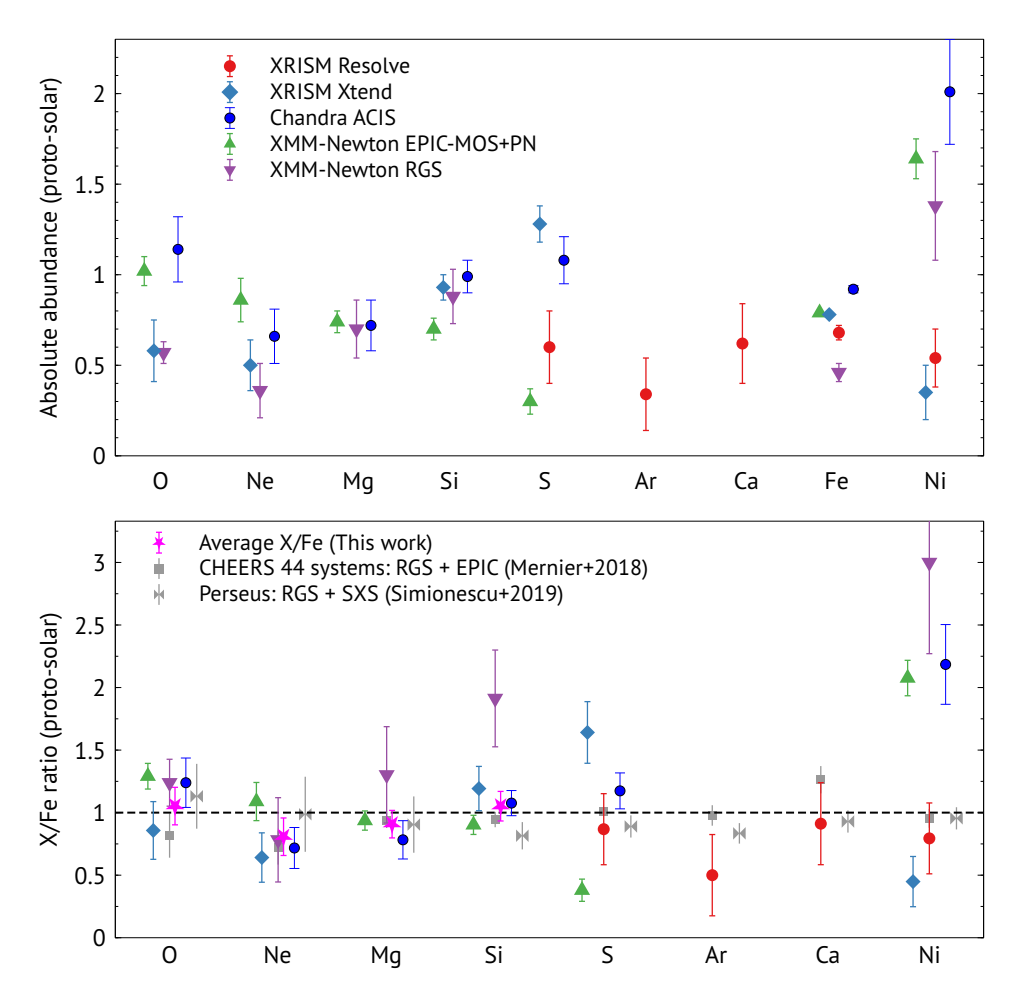


Figure 3. Top: Absolute elemental abundance of different light and heavy elements in the central region of A2029 measured using XRISM (Resolve+Xtend), XMM-Newton (MOS+pn, RGS), and Chandra (ACIS). Bottom: Abundance ratios of different elements with respective to Fe (X/Fe). Grey boxes and tiehorizontals represents the X/Fe for CHEERS samples of clusters/groups (Mernier et al. 2018b) and Perseus cluster (Simionescu et al. 2019).

telescopes, the primary source of bias arises from cross-instrument comparisons. As shown in Figure 3, most X/Fe measurements are consistent across the different instruments. Outlier values were excluded when constructing the average abundance pattern; for example, we omitted the RGS measurement of Si/Fe. To further reduce potential biases, we re-analyzed the archival spectra using the same fitting procedure applied to the XRISM data, rather than adopting chemical abundances reported in the literature.

Any systematic uncertainties in the continuum modeling can significantly affect the derived metal abundances, because, the strength of emission lines is measured relative to the local continuum. In each of the spectral fitting cases discussed in Section 3, the modeled continuum includes contributions from multiple thermal components in the CIE model, background emission (NXB + Sky), and possible power-law emission from a central AGN. All components are subject to absorption

by the Galactic interstellar medium (ISM). Since our focus is limited to the brightest central region of A2029, both AGN and background components do not play a major role and thermal emission from ICM dominates in all cases (de Plaa et al. 2017; Sarkar et al. 2025).

The Galactic absorption column is typically measured via radio surveys and expressed as the atomic hydrogen column density, $N_{\rm H}$ (Kalberla et al. 2005; Willingale et al. 2013). In dense regions of the Galaxy, however, molecular hydrogen and dust can also contribute to the total absorption. As a result, X-ray-derived $N_{\rm H}$ values may differ from those inferred from radio or multiwavelength observations, potentially affecting abundance measurements (e.g., Mernier et al. 2016a; de Plaa et al. 2017). To assess potential systematic uncertainties due to Galactic absorption, we varied the $N_{\rm H}$ value by $\pm 10\%$ from the adopted baseline of $N_{\rm H} = 3 \times 10^{20}$ cm⁻² (HI4PI Collaboration et al. 2016). Since the XRISM/Resolve energy band is restricted to

> 2 keV, it is less sensitive to Galactic absorption effects than other instruments such as RGS. However, these variations in $N_{\rm H}$ had no significant impact on the bestfit parameters, as reported in Table 2.

5. DISCUSSION

5.1. Cluster core enrichment

In this work, we measure the chemical abundances of several elements in the core of A2029 using XRISM (Resolve and Xtend). The exceptional spectral resolution of Resolve allows us to resolve individual emission lines, enabling robust abundance measurements of elements such as S, Ar, Ca, Fe, and Ni. However, because the closed gate valve prevents Resolve from providing spectral sensitivity below 2.0 keV, we supplement the XRISM data with archival XMM-Newton (EPIC and RGS) and Chandra (ACIS) observations. These instruments provide coverage below 2.0 keV, allowing reliable measurements of lighter elements including O, Ne, Mg, and Si. Together, this joint analysis demonstrates the power of combining XRISM with existing observatories, yielding robust abundance constraints for nine elements in total. Among these, Ar, Ca, Fe, and Ni predominantly originate from Type Ia supernovae, while O, Ne, and Mg are mainly produced in core-collapse supernovae.

Since absolute abundances may depend on the instrumental and other systematic effects (e.g., temperature structures), we focus on deriving abundance ratios relative to Fe (X/Fe). Figure 3 presents the resulting X/Fe ratios at A2029 core. Previous studies by Mernier et al. (2016a) and de Plaa et al. (2017) reported X/Fe ratios for A2029 within $0.2R_{500}$ and $0.05R_{500}$ using EPIC and RGS. Our independently derived X/Fe ratios from EPIC and RGS, such as O/Fe ($\sim 1.3 \pm 0.2$), Ne/Fe $(\sim 0.8 \pm 0.3)$, Mg/Fe $(\sim 0.9 \pm 0.1)$, Si/Fe $(\sim 0.9 \pm 0.1)$, and S/Fe ($\sim 0.4 \pm 0.1$)—are consistent with those re-The main difference arises in Ni/Fe: earlier CCD-based analyses obtained significantly higher values than our XRISM measurements. This discrepancy likely stems from the limited spectral resolution of CCD instruments, which prevents robust Ni/Fe constraints because the Ni-K lines remain unresolved. In addition, the high-energy band around the Ni-K transitions is strongly influenced by instrumental background, as the cluster emission drops steeply at these energies. In contrast, Resolve clearly resolves the Ni-K line (see Figure 2), allowing a precise abundance determination. Consistently, Xtend—unlike Chandra and EPIC—benefits from a lower particle background, yielding robust Ni abundance.

The similarity of Fe abundance patterns in massive clusters (Urban et al. 2017) and galaxy groups (Sarkar et al. 2022) at large radii indicates a common early enrichment process predating gravitational collapse. This similarity, and the large mass of diffuse metals compare to the number of stars in present day cluster galaxies, suggests that cluster and group atmospheres were enriched between 3 < z < 10 prior to the formation of clusters (e.g., Loewenstein 2001; E Blackwell et al. 2021). The supernova ejecta was subsequently transported and mixed into the protocluster gas since $z \sim 3$ by large-scale radio jets and galactic winds.

In contrast, the pronounced central abundance peaks observed in massive cool-core clusters are generally attributed to metal enrichment from the brightest cluster galaxy (BCG). Most BCGs are quiescent, appearing red and dead, with their present-day star formation rates on the order of $\sim 0.1~M_{\odot}{\rm yr}^{-1}$. Cooling flow systems, however, exhibit elevated activity, with star formation rates reaching a few $M_{\odot}{\rm yr}^{-1}$, and in rare, extreme cases, as high as several hundred $M_{\odot}{\rm yr}^{-1}$ (McDonald et al. 2012, 2018). In these systems, enhanced light elements are expected in the central regions reflecting enhanced core collapse supernova activity.

Despite being a strong cooling flow, optical observations of A2029's central cD galaxy, IC 1101, have obtained only an upper limit on the central H α luminosity of $< 4.4 \times 10^{39}$ erg s⁻¹. This upper limit implies a visible star formation rate of $< 0.03 M_{\odot}$ yr⁻¹ (McDonald et al. 2010; Hicks et al. 2010; McNamara & Nulsen 2012). The chemical enrichment in the cluster core is therefore thought to be dominated by SNIa with long delay times, supplemented to a lesser degree by metalrich stellar winds. AGN-driven uplift, on the other hand, redistributes metals produced by both SNcc and SNIa that locked up in the stars and the gas in the BCG. SNIa explosions are believed to dominate the majority of Fe and Ni enrichment in clusters.

Abundances of elements heavier than S in A2029 core are consistent with those of the Perseus cluster near NGC 1275 (Hitomi Collaboration et al. 2017), which both lie near the Solar values. This is true despite the very different star formation histories in NGC 1275 and IC 1101. NGC 1275 is presently forming stars at $\sim 10~{\rm M}_{\odot}~{\rm yr}^{-1}$. This would lead to enhancements both in light and heavy elements due to enhanced SNcc in NGC 1275 compared to IC 1101, although SNcc preferentially produce lighter elements that Resolve is not sensitive to. XRISM has revealed abundances in the Centaurus cluster which are above those of the Perseus cluster and the solar value (Mernier et al. 2025, submitted).

The average abundance pattern of the elements in A2029 core, relative to Mg provides a useful comparison to the stellar abundance pattern in Milky Way from the APOGEE surveys (e.g., Hayden et al. 2015; Weinberg et al. 2019). In the Galactic disk, X/Mg ratios derived from APOGEE data shows that α -elements such as O, Si, S, and Ca track Mg closely, while Fe-peak elements like Ni increase with Mg due to the delayed contribution of SNIa. The near-solar Mg/Fe ratio at A2029 center therefore imply a well-mixed enrichment by both SNIa and SNcc, similar to the late-time regime of the Milky Way's thin disk. The sub-solar S/Mg, Ar/Mg, Ca/Mg, and Ni/Mg ratios at A2029 center may arise from differences in integrated SNe yields, where certain elements are produced less efficiently in SNcc or SNIa in cluster galaxies, perhaps indicating time dependent or nonuniversal SN yields. These sub-solar ratios may also, however, be influenced by cross-instrumental biases.

5.2. SNIa and SNcc contributions in metal enrichment

We compare the measured X/Fe ratios in the core of A2029 with predictions from various SNe yield models to draw a clear picture of the enrichment history of ICM. Lighter elements such as O, Ne, and Mg, are primarily synthesized in SNcc, while heavier elements including Ar, Ca, Fe, and Ni are largely produced by SNIa. Thus, the observed X/Fe ratios provide a direct and powerful diagnostic for disentangling the relative contributions of SNcc and SNIa. For this analysis, we constructed composite X/Fe ratios at A2029 center—O-Si/Fe derived from RGS, Xtend, Chandra, and EPIC, and S-Ni/Fe from Resolve—and fitted them with a range of SNcc yields and four sets of SNIa models within abunfit§(Mernier et al. 2016b). For the SNcc models, we explored several initial metallicity options, including 0-0.02 solar (Nomoto et al. 2006; Chieffi & Limongi 2004) and up to 0.05 solar (Nomoto et al. 2013). In each case, a Salpeter initial mass function (IMF; Salpeter 1955) was assumed. The four sets of SNIa models considered represent different explosion mechanisms: pure deflagration, delayed detonation, singledegenerate, and double-degenerate scenarios. The resulting best-fit SNe yield combinations, along with the observed X/Fe ratios in the core of A2029, are shown in Figure 4.

We find that the SNcc yield model of Nomoto et al. (2013) with an initial progenitor metallicity of $Z_{\rm init} = 0.001$ provides the best match to the measured enrichment pattern in all four fitting cases. Additionally, for

the SNIa contribution, the double-degenerate yield from detonative sub-Chandrasekhar-mass white dwarf (WD) explosions (Pakmor et al. 2012) reproduces the overall observed abundance pattern best in the core of A2029, with $\chi^2/\text{dof} = 2.2/7$ (see Figure 4) The inferred SNIa-to-total-SNe (SNIa/SNe) fraction is $\sim 30\%$. In this particular SNIa scenario, two WDs with masses of 1.1 M_{\odot} and 0.9 M_{\odot} undergo a violent merger (without forming an accretion disk), leading to a pure detonation explosion.

We also tested several alternative SNIa yield models based on different explosion mechanisms. The best-fit 3D pure deflagration SNIa model from Fink et al. (2014), when combined with the SNcc model, fails to reproduce the observed Si/Fe and Ca/Fe ratios, yielding a poor fit with $\chi^2/\text{dof} = 13.9/7$. This model also predicts a supersolar Ni/Fe ratio, which is clearly inconsistent with our measurements in the core of A2029. Furthermore, it implies a SNIa/SNe fraction of $\sim 45\%$.

Similarly, the best-fit 3D delayed-detonation SNIa model by (Seitenzahl et al. 2013) better reproduces the observed Ni/Fe ratio relative to the deflagration model, but still fails to reproduce the Si/Fe and Ca/Fe ratios in the A2029 core, with a fit statistic of $\chi^2/\text{dof} = 11.7/7$. The derived SNIa/SNe fraction is $\sim 22\%$. These findings reinforce earlier results by Mernier et al. (2016b), who showed—using the CHEERS sample of 44 clusters and groups—that pure deflagration and delayed-detonation SNIa models fail to reproduce the observed ICM abundance patterns. However, our analysis with XRISM's significantly improved spectral resolution compared to previous CCD-based instruments, provides an independent and more precise confirmation of these conclusions.

We further tested an additional SNIa explosion scenarios: the single-degenerate channels. The best-fit single-degenerate model from Sim et al. (2010), in which a carbon–oxygen white dwarf accretes material from a non-degenerate stellar companion, fails to reproduce the observed Ni/Fe ratio in the core of A2029, yielding a poor fit with $\chi^2/\text{dof} = 17.4/7$. The best-fit SNIa/SNe fraction is ~27%. This result provides strong evidence that the single-degenerate channel is unlikely to be the dominant progenitor pathway for SNIa enrichment in this system.

Among all SNIa yield models considered, the double-degenerate scenario, when combined with the SNcc yields from Nomoto et al. (2013) better reproduces the observed abundance pattern at A2029 core. This result contrasts with the findings of Mernier et al. (2016b), who concluded that detonative sub-Chandrasekhar white dwarf explosions are unlikely to be the dominant SNIa channel in galaxy clusters. A key factor contributing

[§] https://github.com/mernier/abunfit

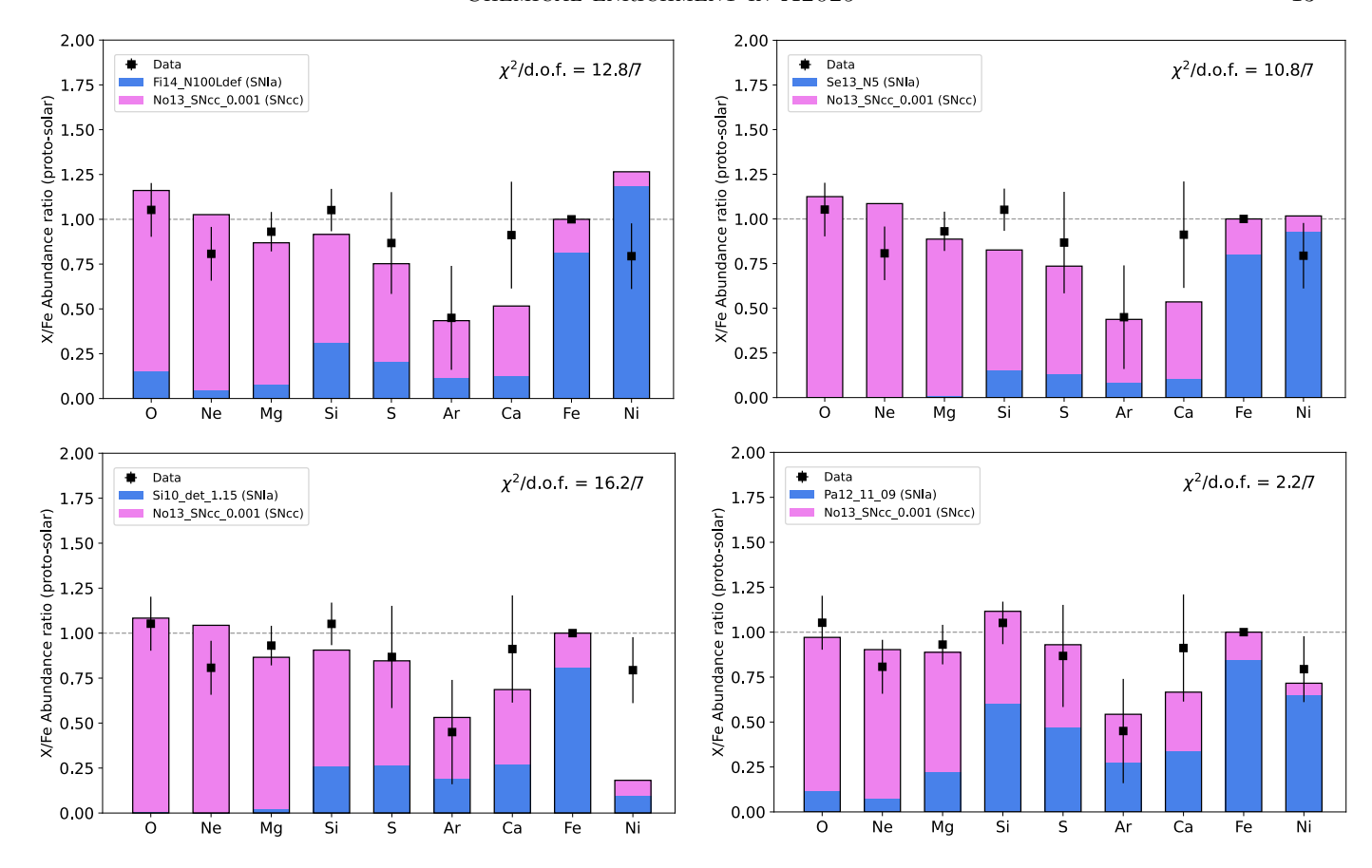


Figure 4. Average elemental abundance ratios of different elements at A2029 center (black data) fitted with SNcc (magenta; Nomoto et al. 2013) and SNIa (blue) yield models. Top-Left: SNIa yield assuming a pure deflagration explosion mechanism (Fink et al. 2014), top-right: SNIa yield assuming a delayed-detonation explosion mechanism (Seitenzahl et al. 2013), bottom-left: SNIa yield assuming a single-degenerate explosion mechanism (Sim et al. 2010), and bottom-right: SNIa yield assuming a double-degenerate explosion mechanism (Pakmor et al. 2012).

to this discrepancy may be the super-solar Ni/Fe ratios reported in the CHEERS sample, which favored deflagration or hybrid deflagration + delayed-detonation models that produce larger amounts of Ni. Measuring Ni abundances with CCD instruments is inherently difficult due to limited spectral resolution and high instrumental background at the energies of Ni–K transitions. As a result, those earlier Ni/Fe measurements may carry substantial systematic uncertainties. Our results, based on XRISM's high-resolution spectroscopy, suggest that the double-degenerate channel as a more plausible dominant SNIa progenitor channel in A2029.

5.3. Excess Calcium abundance

Despite overall good agreement, as shown in Figure 4, the double-degenerate SNIa yield model from Pakmor et al. (2012), combined with the SNcc model from Nomoto et al. (2013), struggles to reproduce the observed Ca/Fe ratio in the core of A2029. Similar, elevated Ca/Fe ratios relative to standard SN yield predictions have been reported in several previous studies

(e.g., Werner et al. 2006; de Plaa et al. 2007; Mernier et al. 2015, 2016a). One possible explanation for the excess Ca in the ICM is the contribution from Ca-rich gap transients, as proposed by Mulchaey et al. (2014). These events are identified as peculiar Type Ib/Ic SNe (e.g., Lunnan et al. 2017) and are believed to originate from helium-accreting white dwarfs rather than core-collapse progenitors (e.g., Waldman et al. 2011; Foley 2015; Zenati et al. 2023). Ca-rich gap transients are characterized by calcium-dominated nebular spectra and unusually high photospheric expansion velocities (Kasliwal et al. 2012). These Ca-rich gap transients tend to explode far from their host galaxies, making it easier for their ejecta to escape and become well mixed into the surrounding ICM (e.g., Yuan et al. 2013).

Motivated by this, we tested a model that adds the Ca-rich gap transient yield from Waldman et al. (2011) to our best-fit combination of the Pakmor et al. (2012) SNIa and Nomoto et al. (2013) SNcc models. As shown in Figure 5, adding a Ca-rich gap supernova component improves the match to the observed Ca/Fe ratio. This

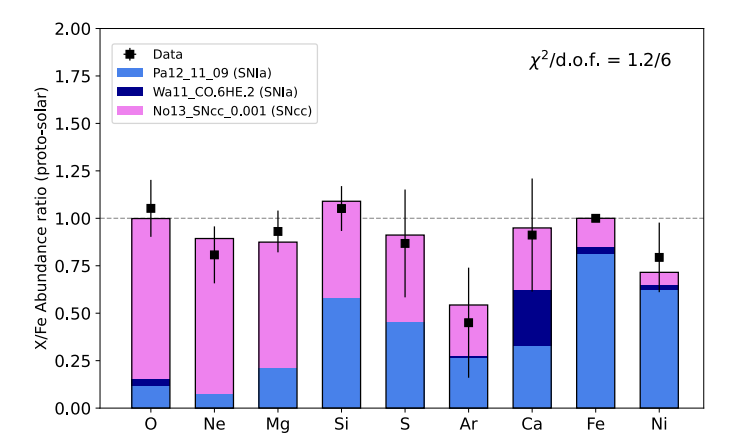


Figure 5. Average elemental abundance ratios of different elements at A2029 center (black data) fitted with SNcc (magenta; Nomoto et al. 2013) and SNIa yield assuming a double-degenerate explosion mechanism (Pakmor et al. 2012) and Ca-gap transients (Waldman et al. 2011).

modification results in a noticeably better overall fit, with an F-test p-value of approximately 0.06 when compared to the one SNIa (double-degenerate) + one SNcc model. Our results clearly indicate a complex chemical enrichment history in the core of A2029. Hitomi observations of the Perseus Cluster (Simionescu et al. 2019) also revealed elevated Ca abundances, which have been interpreted as possible evidence for contributions from Ca-rich gap transients.

Finally, we note that SNe yield models suffer from significant uncertainties up to a factor of 2 (Wiersma et al. 2009), therefore the excess Ca/Fe at A2029 center should be interpreted with caution. We need more deep XRISM observations of galaxy clusters and higher quality SNe yield models to further explore ICM enrichment. Additionally, the derived SNe yield models represent effective, time-averaged mixtures rather than exact combinations of individual SNcc and SNIa events. In reality, the enrichment history involves evolving IMFs, progenitor masses, and explosion channels over cosmic time, making the true picture more complex than the fitted model implies.

6. SUMMARY

We have measured chemical abundance pattern of several α and Fe-peak elements within the core of A2029 (3' × 3') using XRISM and archival observations from XMM-Newton and Chandra. Our main findings are summarized below.

- The two-temperature (2T CIE) model fit from Resolve shows cooler and hotter gas components that

- are consistent with those measured by Xtend and EPIC. Although RGS is limited to the 0.2–2 keV band and is more sensitive to hotter gas, its measured hotter gas temperature $(4.40^{+0.11}_{0.10} \text{ keV})$ is consistent with the cooler components found by the other instruments.
- We have constructed an average X/Fe pattern for the A2029 core by combining measurements from multiple instruments. For the S/Fe, Ar/Fe, Ca/Fe, and Ni/Fe abundance ratios, we primarily leverage Resolve's superior spectral resolution and sensitivity. Abundance ratios for O/Fe and Ne/Fe are averaged from Xtend+RGS and Xtend+RGS+EPIC+Chandra, respectively. Mg/Fe and Si/Fe ratios are averaged from EPIC+Chandra and Xtend+EPIC+Chandra, respectively.
- By comparing the average X/Fe ratios with various SNcc and SNIa yield models, we find that SNcc yield model from Nomoto et al. (2013), assuming an initial progenitor metallicity of $Z_{\rm init}=0.001$, combined with a SNIa model involving sub- $M_{\rm Ch}$ WD detonation in a double-degenerate system (Pakmor et al. 2012), provides the best overall match to the observed abundance pattern in the cluster core.
- We observe an excess in Ca abundance in the core of A2029 that cannot be reproduced by the double-degenerate SNIa yield model. When we include a Ca-rich gap component (Waldman et al. 2011) in the SNe modeling, the agreement with the observed Ca/Fe ratio significantly improves.

ACKNOWLEDGEMENT

We sincerely thank the anonymous referee for their helpful suggestions and comments. We gratefully acknowledge the dedicated efforts of the many engineers and scientists whose hard work over the years made the XRISM mission possible. AS and EDM acknowledges support from NASA grants 80NSSC20K0737 and 80NSSC24K0678. MS acknowledges support from NASA grant 80NSSC23K0650. LL acknowledges the financial contribution from the INAF grant 1.05.12.04.01. S.E. acknowledges the financial contribution from Theory Grant / Bando INAF per la Ricerca Fondamentale 2024 on "Constraining the non-thermal pressure in galaxy clusters with high-resolution X-ray spectroscopy" (1.05.24.05.10). This paper employs a list of Chandra datasets, obtained by the Chandra X-ray Observatory, contained in DOI: 10.25574/cdc.499

REFERENCES

- Arnaud, K. A. 1996, in Astronomical Society of the Pacific Conference Series, Vol. 101, Astronomical Data Analysis Software and Systems V, ed. G. H. Jacoby & J. Barnes, 17
- Bildsten, L., Shen, K. J., Weinberg, N. N., & Nelemans, G. 2007, ApJL, 662, L95, doi: 10.1086/519489
- Cash, W. 1979, ApJ, 228, 939, doi: 10.1086/156922
- Chakraborty, P., Ferland, G. J., Chatzikos, M., Guzmán,
 F., & Su, Y. 2020a, ApJ, 901, 68,
 doi: 10.3847/1538-4357/abaaab
- —. 2020b, ApJ, 901, 69, doi: 10.3847/1538-4357/abaaac
- Chieffi, A., & Limongi, M. 2004, ApJ, 608, 405, doi: 10.1086/392523
- de Plaa, J., Werner, N., Bleeker, J. A. M., et al. 2007, A&A, 465, 345, doi: 10.1051/0004-6361:20066382
- de Plaa, J., Kaastra, J. S., Werner, N., et al. 2017, A&A, 607, A98, doi: 10.1051/0004-6361/201629926
- E Blackwell, A., Bregman, J. N., & Snowden, S. L. 2021, arXiv e-prints, arXiv:2105.04638. https://arxiv.org/abs/2105.04638
- Fink, M., Röpke, F. K., Hillebrandt, W., et al. 2010, A&A, 514, A53, doi: 10.1051/0004-6361/200913892
- Fink, M., Kromer, M., Seitenzahl, I. R., et al. 2014, MNRAS, 438, 1762, doi: 10.1093/mnras/stt2315
- Foley, R. J. 2015, MNRAS, 452, 2463, doi: 10.1093/mnras/stv789
- Fujita, Y., Fukushima, K., Sato, K., Fukazawa, Y., & Kondo, M. 2025, PASJ, doi: 10.1093/pasj/psaf089
- Fukushima, K., Kobayashi, S. B., & Matsushita, K. 2023, ApJ, 953, 112, doi: 10.3847/1538-4357/ace16a
- Gastaldello, F., Simionescu, A., Mernier, F., et al. 2021, Universe, 7, 208, doi: 10.3390/universe7070208
- Guillochon, J., Dan, M., Ramirez-Ruiz, E., & Rosswog, S. 2010, ApJL, 709, L64, doi: 10.1088/2041-8205/709/1/L64
- Hayden, M. R., Bovy, J., Holtzman, J. A., et al. 2015, ApJ, 808, 132, doi: 10.1088/0004-637X/808/2/132
- HI4PI Collaboration, Ben Bekhti, N., Flöer, L., et al. 2016, A&A, 594, A116, doi: 10.1051/0004-6361/201629178
- Hicks, A. K., Mushotzky, R., & Donahue, M. 2010, ApJ, 719, 1844, doi: 10.1088/0004-637X/719/2/1844
- Hitomi Collaboration, Aharonian, F., Akamatsu, H., et al. 2017, Nature, 551, 478, doi: 10.1038/nature24301
- Iben, Jr., I., & Tutukov, A. V. 1984, ApJS, 54, 335, doi: 10.1086/190932

- Ishisaki, Y., Kelley, R. L., Awaki, H., et al. 2022, in Society of Photo-Optical Instrumentation Engineers (SPIE)
 Conference Series, Vol. 12181, Space Telescopes and Instrumentation 2022: Ultraviolet to Gamma Ray, ed. J.-W. A. den Herder, S. Nikzad, & K. Nakazawa, 121811S, doi: 10.1117/12.2630654
- Iwamoto, K., Brachwitz, F., Nomoto, K., et al. 1999, ApJS, 125, 439, doi: 10.1086/313278
- Kalberla, P. M. W., Burton, W. B., Hartmann, D., et al. 2005, AAP, 440, 775, doi: 10.1051/0004-6361:20041864
- Kasliwal, M. M., Kulkarni, S. R., Gal-Yam, A., et al. 2012, ApJ, 755, 161, doi: 10.1088/0004-637X/755/2/161
- Kromer, M., Sim, S. A., Fink, M., et al. 2010, ApJ, 719, 1067, doi: 10.1088/0004-637X/719/2/1067
- Lodders, K., & Palme, H. 2009, Meteoritics and Planetary Science Supplement, 72, 5154
- Loewenstein, M. 2001, ApJ, 557, 573, doi: 10.1086/322256
 Lunnan, R., Kasliwal, M. M., Cao, Y., et al. 2017, ApJ, 836, 60, doi: 10.3847/1538-4357/836/1/60
- Maoz, D., & Mannucci, F. 2012, PASA, 29, 447, doi: 10.1071/AS11052
- Maoz, D., Mannucci, F., & Nelemans, G. 2014, ARA&A, 52, 107, doi: 10.1146/annurev-astro-082812-141031
- McDonald, M., Gaspari, M., McNamara, B. R., & Tremblay, G. R. 2018, ApJ, 858, 45, doi: 10.3847/1538-4357/aabace
- McDonald, M., Veilleux, S., Rupke, D. S. N., & Mushotzky, R. 2010, ApJ, 721, 1262, doi: 10.1088/0004-637X/721/2/1262
- McDonald, M., Bayliss, M., Benson, B. A., et al. 2012, Nature, 488, 349, doi: 10.1038/nature11379
- McNamara, B. R., & Nulsen, P. E. J. 2012, New Journal of Physics, 14, 055023, doi: 10.1088/1367-2630/14/5/055023
- Mernier, F., de Plaa, J., Lovisari, L., et al. 2015, A&A, 575, A37, doi: 10.1051/0004-6361/201425282
- Mernier, F., de Plaa, J., Pinto, C., et al. 2016a, A&A, 592, A157, doi: 10.1051/0004-6361/201527824
- —. 2016b, A&A, 595, A126,doi: 10.1051/0004-6361/201628765
- Mernier, F., Biffi, V., Yamaguchi, H., et al. 2018a, SSRv, 214, 129, doi: 10.1007/s11214-018-0565-7
- Mernier, F., de Plaa, J., Werner, N., et al. 2018b, MNRAS, 478, L116, doi: 10.1093/mnrasl/sly080
- Molendi, S., & Gastaldello, F. 2009, A&A, 493, 13, doi: 10.1051/0004-6361:200810138
- Molendi, S., Ghizzardi, S., De Grandi, S., et al. 2024, A&A, 685, A88, doi: 10.1051/0004-6361/202346918
- Mulchaey, J. S., Kasliwal, M. M., & Kollmeier, J. A. 2014, ApJL, 780, L34, doi: 10.1088/2041-8205/780/2/L34

- Nomoto, K., Kobayashi, C., & Tominaga, N. 2013, ARA&A, 51, 457,
 - doi: 10.1146/annurev-astro-082812-140956
- Nomoto, K., Tominaga, N., Umeda, H., Kobayashi, C., & Maeda, K. 2006, NuPhA, 777, 424, doi: 10.1016/j.nuclphysa.2006.05.008
- Pakmor, R., Kromer, M., Taubenberger, S., et al. 2012, ApJL, 747, L10, doi: 10.1088/2041-8205/747/1/L10
- Pakmor, R., Kromer, M., Taubenberger, S., & Springel, V. 2013, ApJL, 770, L8, doi: 10.1088/2041-8205/770/1/L8
- Plewa, T., Calder, A. C., & Lamb, D. Q. 2004, ApJL, 612, L37, doi: 10.1086/424036
- Renzini, A., & Andreon, S. 2014, MNRAS, 444, 3581, doi: 10.1093/mnras/stu1689
- Ruiter, A. J., & Seitenzahl, I. R. 2025, A&A Rv, 33, 1, doi: 10.1007/s00159-024-00158-9
- Salpeter, E. E. 1955, ApJ, 121, 161, doi: 10.1086/145971
- Sarkar, A., Su, Y., Truong, N., et al. 2022, MNRAS, 516, 3068, doi: 10.1093/mnras/stac2416
- Sarkar, A., Miller, E., Ota, N., et al. 2025, PASJ, 77, S254, doi: 10.1093/pasj/psaf093
- Schellenberger, G., Reiprich, T. H., Lovisari, L., Nevalainen, J., & David, L. 2015, A&A, 575, A30, doi: 10.1051/0004-6361/201424085
- Seitenzahl, I. R., Ciaraldi-Schoolmann, F., Röpke, F. K., et al. 2013, MNRAS, 429, 1156, doi: 10.1093/mnras/sts402
- Shen, K. J., & Bildsten, L. 2009, ApJ, 699, 1365, doi: 10.1088/0004-637X/699/2/1365
- —. 2014, ApJ, 785, 61, doi: 10.1088/0004-637X/785/1/61
- Shen, K. J., Kasen, D., Miles, B. J., & Townsley, D. M. 2018, ApJ, 854, 52, doi: 10.3847/1538-4357/aaa8de
- Sim, S. A., Röpke, F. K., Hillebrandt, W., et al. 2010, ApJL, 714, L52, doi: 10.1088/2041-8205/714/1/L52
- Simionescu, A., Nakashima, S., Yamaguchi, H., et al. 2019, MNRAS, 483, 1701, doi: 10.1093/mnras/sty3220
- Snowden, S. L., Mushotzky, R. F., Kuntz, K. D., & Davis, D. S. 2008, A&A, 478, 615, doi: 10.1051/0004-6361:20077930

- Tashiro, M., Maejima, H., Toda, K., et al. 2020, in Society of Photo-Optical Instrumentation Engineers (SPIE)
 Conference Series, Vol. 11444, Space Telescopes and Instrumentation 2020: Ultraviolet to Gamma Ray, ed.
 J.-W. A. den Herder, S. Nikzad, & K. Nakazawa, 1144422, doi: 10.1117/12.2565812
- Urban, O., Werner, N., Allen, S. W., Simionescu, A., & Mantz, A. 2017, MNRAS, 470, 4583, doi: 10.1093/mnras/stx1542
- Verner, D. A., Ferland, G. J., Korista, K. T., & Yakovlev, D. G. 1996, ApJ, 465, 487, doi: 10.1086/177435
- Waldman, R., Sauer, D., Livne, E., et al. 2011, ApJ, 738, 21, doi: 10.1088/0004-637X/738/1/21
- Weinberg, D. H., Holtzman, J. A., Hasselquist, S., et al. 2019, ApJ, 874, 102, doi: 10.3847/1538-4357/ab07c7
- Werner, N., de Plaa, J., Kaastra, J. S., et al. 2006, A&A, 449, 475, doi: 10.1051/0004-6361:20053868
- Whelan, J., & Iben, Jr., I. 1973, ApJ, 186, 1007, doi: 10.1086/152565
- Wiersma, R. P. C., Schaye, J., Theuns, T., Dalla Vecchia,
 C., & Tornatore, L. 2009, MNRAS, 399, 574,
 doi: 10.1111/j.1365-2966.2009.15331.x
- Willingale, R., Starling, R. L. C., Beardmore, A. P., Tanvir,
 N. R., & O'Brien, P. T. 2013, MNRAS, 431, 394,
 doi: 10.1093/mnras/stt175
- Wilms, J., Allen, A., & McCray, R. 2000, ApJ, 542, 914, doi: 10.1086/317016
- Woosley, S. E., & Kasen, D. 2011, ApJ, 734, 38, doi: 10.1088/0004-637X/734/1/38
- XRISM Collaboration. 2024, arXiv e-prints, arXiv:2408.14301, doi: 10.48550/arXiv.2408.14301
- —. 2025, arXiv e-prints, arXiv:2501.05514. https://arxiv.org/abs/2501.05514
- XRISM Collaboration, Audard, M., Awaki, H., et al. 2025a, arXiv e-prints, arXiv:2505.06533, doi: 10.48550/arXiv.2505.06533
- —. 2025b, arXiv e-prints, arXiv:2508.05067, doi: 10.48550/arXiv.2508.05067
- 2025c, ApJL, 985, L20, doi: 10.3847/2041-8213/add2f6
 Yuan, F., Kobayashi, C., Schmidt, B. P., et al. 2013,
 MNRAS, 432, 1680, doi: 10.1093/mnras/stt591
- Zenati, Y., Perets, H. B., Dessart, L., et al. 2023, ApJ, 944, 22, doi: 10.3847/1538-4357/acaf65